EUROPEAN ORGANIZATION FOR NUCLEAR RESEARCH

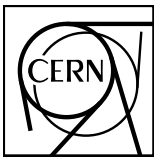

CERN-PH-EP-2015-XXX
Day Month 2015

Λ and K^0_S in jets in p–Pb collisions at $\sqrt{s_{NN}} = 5.02$ TeV

ALICE Collaboration*

Abstract

The production of Λ baryons and K^0_S mesons has been measured separately in hard scattering region and the underlying event in p–Pb collisions at $\sqrt{s_{NN}} = 5.02$ TeV at the LHC. The hard scatterings are selected on an event-by-event basis by jets reconstructed using charged particles with anti$-k_T$ jet finder. The production of the particles is reported depending on the angular distance ΔR from the jet axis for jets with $p_T^{jet} > 10$ GeV/$c$and $p_T^{jet} > 20$ GeV/c.

For small ΔR ($\Delta R < 1.0$) the ratio of Λ to K^0_S associated to jets is found consistent with the expectation of jets fragmenting in vacuum given by PYTHIA event generator. Whereas, the ratio for large ΔR (i.e. the underlying event) shows a maximum (similar to the inclusive distribution in p–Pb collisions) at the intermediate p_T of 2-5 GeV/c.

*See Appendix A for the list of collaboration members

1 Introduction

High-energy heavy ion collisions provide a unique opportunity to study properties of hot and dense QCD medium composed of deconfined partons - the quark-gluon plasma (QGP). The QGP is predicted by the lattice QCD calculations [1–4]. The cross-over transition from hadronic matter to the QGP matter at zero baryochemical potential is expected to take place once the temperature of the matter T_c reaches values of about 150 MeV and/or energy density ε_c of about 0.5 GeV/fm^3 [5, 6]. The measurements indicate that the most violent collisions of lead ions at the LHC at $\sqrt{s_{\rm NN}} = 2.76$ TeV create conditions well above the critical temperature at approximately zero baryochemical potential. The bulk matter created in those collisions can be quantitatively described in terms of hydrodynamic and statistical models. The initial hot and dense partonic matter rapidly expands and cools down, ultimately undergoing a transition to a hadron gas phase [7]. During the expansion phase, collective hydrodynamic flow develops from the initially generated pressure gradients in the strongly interacting system. This results in a characteristic dependence of the shape of the transverse momentum ($p_{\rm T}$) distribution on the particle mass that can be described using a common kinetic freeze-out temperature parameter $T_{\rm kin}$ and a collective average expansion velocity $\langle\beta_{\rm T}\rangle$ [8].

The interpretation of heavy-ion results depends on the understanding of results from smaller collision systems such as proton-proton (pp) or proton-nucleus (pA). Proton-nucleus collisions are intermediate between proton-proton and nucleus-nucleus collisions in terms of system size and number of produced particles. Comparing particle production in pp, pA, and AA reactions has frequently been used to separate initial state effects, linked to the use of nuclear beams or targets, from final state effects, associated to the presence of hot and dense matter. At the LHC, however, the pseudorapidity density of final state particles in pA collisions reaches values which can become comparable to semi-peripheral Au–Au (∼60% most central) and Cu–Cu (∼30% most central) collisions at top RHIC energy [9]. Indeed, the measurements at the LHC in high-multiplicity pp and p–Pb collisions have revealed unexpectedly strong long-range correlations of produced particles [10–15] falsyfying the assumption that final state dense matter effects can be neglected in pA.

Various mechanisms have been proposed to explain the origin of this collective particle production. Both a Color Glass Condensate (CGC) description [16], based on initial state nonlinear gluon interactions, as well as a model based on hydrodynamic flow [17, 18], assuming strong interactions between final state partons or hadrons, can give a satisfactory description of the p–Pb correlation data. However, the modeling of small systems such as p–Pb is complicated because uncertainties related to initial state geometrical fluctuations play a large role and because viscous corrections may be too large for hydrodynamics to be a reliable framework [19].

Results on identified particle production in p–Pb collisions at a nucleon-nucleon center-of-mass energy $\sqrt{s_{\rm NN}} = 5.02$ TeV at the LHC [20] have shown qualitatively similar effects as in AA collisions [21, 22]. In particular the ratio of baryon and meson transverse momentum ($p_{\rm T}$) spectra shows a pronounced maximum at intermediate $p_{\rm T}$. The shape of the ratio has been discussed in terms of an interplay between the radial expansion of the system and produced particles in a common velovity field (collective flow) [8], soft-hard parton recombination [23] and hard parton (jet) hadronization at high $p_{\rm T}$. Concurently the measurements of jets at mid-rapidty originating from fragmentation of highly-virtual partons produced in hard scatterings within the pA collisions [24, 25] have revealed that the final state nuclear effects such as shadowing and gluon saturation (CGC) [26, 27], or multiple scatterings and hadronic re-interactions in the initial and

final state [28, 29] are not significant. In particular, the suppression related to the creation of the QGP in AA collisions was not observed in p–Pb collisions [30–34].

In this letter we report on the measurement of Λ and $\overline{\Lambda}$and $K^0_S$where the production of particles is studied separately within the region associated to a hard scattering and the remainder of the event (the so called "underlying event"). The hard scatterings are identified by selecting an energetic jet ($p_T^{jet} > 10 or 20 GeV/c$) reconstructed with the anti-k_T algorithm with the resolution parameter R of 0.2, 0.3 and 0.4. The Λ-to-K^0_S ratio associated to jets is reported as a function of particle momentum and as a function of their distance to the jet axis.

2 Data analysis

2.1 Data sample

The data used for this analysis was recorded by ALICE detector [35] during the LHC p–Pb run at $\sqrt{s_{NN}} = 5.02$ TeV in the beginning of 2013. Since the 2-in-1 magnet design of the LHC [36], the energy of the two beams are not independent and their ratio is fixed to equal to the ratio of the charge/mass ratios of each beam. Consequently, the nucleon-nucleon center-of-mass system (cms) was moving with a rapidity of $\Delta y_{NN} = 0.465$ in the direction of the proton beam. The used data was collected for the beam configuration, in which the Pb beam circulated in the "counter-clockwise" direction traveling from negative to positive rapidity.

The ALICE apparatus [35] consists of central barrel detectors covering the pseudo-rapidity interval $|\eta| < 0.9$, a forward muon spectrometer covering the pseudo-rapidity interval $-4.0 < \eta_{lab}\eta < -2.5$, and a set of detectors at forward and backward rapidities used for triggering and event characterization.

Tracking and particle identification are performed using the information provided by the Inner Tracking System (ITS) [37], the Time Projection Chamber (TPC) [38] and the Time Of Flight (TOF) [39] detectors, that have full azimuthal coverage in the pseudo-rapidity interval $|\eta_{lab}| < 0.9$. These central barrel detectors are located inside a large solenoidal magnet, which provides a magnetic field of 0.5 T along the beam direction (z axis in the ALICE reference frame).

ITS is composed of six cylindrical layers of silicon detectors, with radial distances from the beam axis ranging from 3.9 cm to 43.0 cm. The two innermost layers, with average radii of 3.9 cm and 7.6 cm, are equipped with Silicon Pixel Detectors (SPD). The two SPD layers, covering the pseudo-rapidity ranges of $|\eta_{lab}| < 2.0$ and $|\eta_{lab}| < 1.4$ respectively, have 1200 SPD readout chips. The two intermediate layers are made of Silicon Drift Detectors (SDD), while Silicon Strip Detectors (SSD) equip the two outermost layers. The high spatial resolution of the silicon sensors, together with the low material budget (on average 7.7% of a radiation length for tracks crossing the ITS perpendicularly to the detector surfaces, i.e. $\eta_{lab} = 0$) and the small distance of the innermost layer from the beam vacuum tube, allow for the measurement of the track impact parameter in the transverse plane (d_0), i.e. the distance of closest approach of the track to the primary vertex in the plane transverse to the beam direction, with a resolution better than 75 μm for transverse momenta $p_T > 1$ GeV/c [37]. The SPD provides also a measurement of the multiplicity of charged particles produced in the collision based on track segments (tracklets) built by associating pairs of hits in the two SPD layers.

At larger radii ($85 < r < 247$ cm), a 510 cm long cylindrical TPC provides track reconstruction

with up to 159 three-dimensional space points per track, as well as particle identification via the measurement of the specific energy deposit $\mathrm{d}E/\mathrm{d}x$ in the gas. The charged particle identification capability of the TPC is supplemented by the TOF, which is equipped with Multi-gap Resistive Plate Chambers (MRPCs) located at radial distances between 377 and 399 cm from the beam axis. The overall TOF resolution including the uncertainty on the time at which the collision took place, and the tracking and momentum resolution was about 160 ps for the data-taking period considered in these analyses.

The V0 detector [40], used for triggering and for estimating the multiplicity of charged particles in the forward rapidity region, consists of two arrays of 32 scintillator tiles each, placed around the beam vacuum tube on either side of the interaction region at $z = -90$ cm and $z = +340$ cm. The two arrays cover the pseudo-rapidity intervals $-3.7 < \eta_{\mathrm{lab}} < -1.7$ (VZERO-C) and $2.8 < \eta_{\mathrm{lab}} < 5.1$ (VZERO-A), respectively. In addition two Zero Degree Calorimeters (ZDCs) located at $+112.5$ m (ZNA) and -112.5 m (ZNC) from the interaction point were used for beam background rejection and an alternative estimator of the event activity.

2.2 Event selection

The minimum-bias trigger signal was provided by the VZERO [40] counters, the VZERO-A in Pb beam direction and the VZERO-C in proton beam direction covering the pseudo-rapidity $2.8 < \eta_{\mathrm{lab}} < 5.1$ and $-3.7 < \eta_{\mathrm{lab}} < -1.7$, respectively. The signal amplitude and arrival time collected in each tile of the detectors were recorded. A coincidence of signals in both VZERO-A and VZERO-C detectors was required to remove contamination from single diffractive and electromagnetic events [41]. The resolution of the arrival time is better than 1 ns, allowing discrimination of beam–beam collisions from background events produced outside of the interaction region. In the offline analysis, background was further suppressed by the time information recorded in two neutron Zero Degree Calorimeters (ZDCs), which located at $+112.5$ m (ZNA) and -112.5 m (ZNC) from the interaction point. A dedicated quartz radiator Cherenkov detector (T0) [39] provided a measurement of the event time of the collision.

The events were further selected by requiring a reconstructed vertex within $10cm$ ($v_z < 10$ cm) along beam axis and that the vertices built from SPD tracklets and from the global tracks (combining information of ITS and TPC) were compatible. The analysis requires a reconstructed vertex, which is the case for 98.2% of the events selected by the trigger and the total number of events retained in the analysis was 96 M.

2.3 Charged particle reconstruction

Charged-hadron identification in the central barrel was performed with the ITS, TPC and TOF detectors. The drift and strip layers of the ITS provide a measurement of the specific energy loss with a resolution of about 10%. In a standalone tracking mode, the identification of pions, kaons, and protons is thus extended down to respectively 0.1, 0.2, 0.3 GeV/c in p_{T}. The TPC provides particle identification at low momenta via specific energy loss $\mathrm{d}E/\mathrm{d}x$ in the fill gas by measuring up to 159 samples per track with a resolution of about 6%. The separation power achieved in p–Pb collisions is identical to that in pp collisions [42]. Further outwards at about 3.7 m from the beam line, the TOF array allows identification at higher p_{T} measuring the particle speed with the time-of-flight technique. The total time resolution is about 85 ps for events in the multiplicity classes from 0% to $\sim$ 80%. In more peripheral collisions, where multiplicities are similar to pp, it decreases to about 120 ps due to a worse start-time (collision-time) resolu-

tion [42]. The start-time of the event was determined by combining the time estimated using the particle arrival times at the TOF and the time measured by the T0 detector.

Since the p–Pb center-of-mass system moved in the laboratory frame with a rapidity of $y_{\rm NN} = -0.465$, the nominal acceptance of the central barrel of the ALICE detector was asymmetric with respect to $y_{\rm CMS} = 0$. In order to ensure good detector acceptance and optimal particle identification performance, tracks were selected in the rapidity interval $0 < y_{\rm CMS} < 0.5$ in the nucleon-nucleon center-of-mass system. Event generator studies and repeating the analysis in $|y_{\rm CMS}| < 0.2$ indicate differences between the two rapidity selections smaller than 2% in the normalization and 3% in the shape of the transverse momentum distributions.

2.4 Jet reconstruction

The jet reconstruction in this letter follows the analysis of the inclusive charged particle jet spectrum presented in [24]. Here only a brief review of the most relevant points is presented. Charged particle tracks are reconstructed as tracks in the ITS and the TPC which cover the full azimuth and $|\eta_{\rm lab}| < 0.9$. Tracks with $p_{\rm T} > 0.15$ GeV/c and within a pseudorapidity interval $|\eta_{\rm lab}| < 0.9$ were used as input to the jet reconstruction. The overall efficiency for charged particle detection, including the effect of tracking efficiency as well as the geometrical acceptance, is 70% at $p_{\rm T} = 0.15$ GeV/c and increases to 85% at $p_{\rm T} = 1$ GeV/c and above. Add the DCA cut to vertex and the consequence that the L/K decay products do not contribute to the jet energy. . The jets were reconstructed using the anti-$k_{\rm T}$ algorithm [43] from the FastJet package [44, 45] with resolution parameters of $R = 0.2$, 0.3 and 0.4. Only the jets where the jet-axis was found within the acceptance window $|\eta_{\rm lab}| < 0.35$ that is fully overlapping with the acceptances of both charged particle tracks ($|\eta_{\rm lab}| < 0.9$) and $\rm V^0$s ($|\eta_{\rm lab}| < 0.75$, see section 2.5 for the details) for any of the jet resolution parameters. The jet transverse momentum is calculated by FastJet using the $p_{\rm T}$ recombination scheme.

In general the transverse momentum density of the background originating from the underlying event and/or pile-up (particles not associated to the hard scattering) contributes to the jet energy reported by the jet finder. The correction of the jet energy scale accounting for the background energy can be estimated on event-by-event basis using the median of all jet candidate clusters $p_{\rm T,ch\,jet}$ reconstructed with the $k_{\rm T}$ algorithm per unit area [46]. This method has been used in the analysis of Pb–Pb events [33, 47]. In this analysis, an estimate adequate for the more sparse environment of p–Pb collisions was employed [24]. The resulting mean of the background $p_{\rm T}$ density $\langle \rho^{\rm ch} \rangle = 1.02$ GeV/$c\times$rad^{-1} with a standard deviation of $\sigma(\rho^{\rm ch}) = 0.91$ GeV/$c\times$rad^{-1} for unbiased events and, $\langle \rho^{\rm ch} \rangle = 2.2$ GeV/$c\times$rad^{-1} and $\sigma(\rho^{\rm ch}) = 1.47$ GeV/$c\times$rad^{-1} for events containing an energetic jet with $p^{raw}_{\rm T,ch\,jet} > 20$ GeV/c [24].

We need to comment on: a) the jet efficiency for $p_{\rm T} < 20$ GeV/c. Not in the cited paper. Below some text from the jet in p–Pb paper.

2.5 Λ ($\overline{\Lambda}$) and $\rm K^0_S$ reconstruction

The reconstruction the $\rm V^0$particles ($\rm K^0_S$ Λ, and $\overline{\Lambda}$) is follows the analysis in [20] with the exception of the rapidity selection of the particles and their decay products.

See how much details is needed - since all follows from [20].

The $p_{\rm T}$ differential yields of $\rm V^0$particles were extracted via the invariant mass method described

Selection variable	Cut value
2D decay radius	> 0.50 cm
Daughter track DCA to prim. vertex	> 0.06 cm
DCA between daughter tracks	$< 1.0\ \sigma$
Cosine of pointing angle (K^0_S)	> 0.97
	($< 1\%$ signal loss)
Cosine of pointing angle (Λ and $\bar{\Lambda}$)	> 0.995
	($< 1\%$ signal loss)
Proper lifetime (K^0_S)	< 20 cm
Proper lifetime (Λ and $\bar{\Lambda}$)	< 30 cm
K^0_S mass rejection window (Λ and $\bar{\Lambda}$)	± 10 MeV/c
Λ and $\bar{\Lambda}$ mass rejection window (K^0_S)	± 5 MeV/c

Table 1: V^0 topological selection cuts (DCA: distance-of-closest approach). check if the cos theta p_T dependent(?)

in [20]. Table 1 presents the topological cuts applied on the candidate tracks of the decays daughters. The V^0 particles, K^0_S and Λ ($\overline{\Lambda}$), were identified exploring the characteristics of their weak decay topologies in the channels $K^0_S \to \pi^+\pi^-$ and $\Lambda(\overline{\Lambda}) \to p\pi^-(\bar{p}\pi^+)$, which have branching ratios of 69.2% and 63.9%, respectively [48]. The selection criteria used to define V^0 candidates are listed in table 1 (see [49] for details). The V^0 decay-product tracks are selected in the acceptance window $|\eta_{\rm lab}| < 0.8$, only the candidates reconstructed in $|\eta_{\rm lab}| < 0.75$ are retained to keep $> 50\%$ of acceptance and reconstruction efficiency at plateau around $\eta_{\rm lab} = 0$ (is it clear or is it needed?) . A five-standard-deviation particle-identification cut was applied on the difference between dE/dx in the TPC and that defined by parameterized Bethe-Bloch curve for the V^0 decay-product tracks. In addition, by using proper lifetime selection coupled to cosine of pointing angle ($\cos\theta_{\rm pointing}$) selection of $\cos\theta_{\rm pointing} > 0.995$, a significant amount of secondary Λ ($\overline{\Lambda}$) generated in detector material are removed. The residual contamination entering the selections was $< 1\%$ and was neglected [21]. The yield of V^0 signal is extracted from the invariant mass, $M_{\rm inv}$, distribution of identified V^0 candidates subtracting the combinatory background from the peak region with the bin counting method. The background was determined by fitting first order polynomials to sideband regions. The signal region and sidebands are defined on the basis of the p_T-dependent mass resolution as the windows in $|M_{\rm inv} - M_0| < 6\sigma$ and $6\sigma < |M_{\rm inv} - M_0| < 12\sigma$, respectively, where M_0 and σ are the mean and width of invariant mass distribution extracted by the Gaussian fit.

2.6 V^0–jet matching

In this analysis that the selection cuts for primary particle tracks used for the jet reconstruction are not compatible with the V^0 candidate tracks. Only a small fraction (<1%) of V^0 candidate daughter tracks enter the jet reconstruction. To obtain the yield of V^0 particles within a jet cone the V^0 particles are matched to a hard scattering based on their distance in the pseudo-rapidity and azimuthal angle plane. In general, a particle that is within the radius R from the jet axis is considered as matched to a given jet. In p–Pb collisions the probability for a particle to

match to two jets with $p_{\mathrm{T}} > 10 GeV/c$ is less than 1% (check number) and in those cases the higher energy jet is preferred. say what fraction The procedure for extraction of the yield of V^0 particles associated a jet within a cone R (JC V^0) can be summarized as follows:

- the V^0 candidates are selected with the cuts defined within the acceptance of $|\eta| < 0.75$;
- the candidates are associated to the hard scattering with a distance cut in pseudo-rapidity and azimuthal angle plane ($\eta_{\mathrm{lab}} \times \varphi$): $\Delta R_{\mathrm{V}^0-\mathrm{jet}} < R$, where

$$\Delta R_{\mathrm{V}^0-\mathrm{jet}} = \sqrt{(\eta_{\mathrm{lab}}^{\mathrm{jet}} - \eta_{\mathrm{lab}}^{\mathrm{V}^0})^2 - (\varphi^{\mathrm{jet}} - \varphi^{\mathrm{V}^0})^2} \quad (1)$$

  is the distance between the particle candidate and jet axis;
- for each p_{T} interval of the V^0 candidates matching at least one jet within the radius R an invariant mass distribution (needs a demo figure?) is constructed and the combinatorial background interpolated from the yield in side bands around the mass peak region defined by the width and mean of the peak for the inclusive V^0 candidates;
- finally, the JC yield is corrected for the contribution of particles from the underlying event (UE) (various estimators of V^0 particles of the UE are discussed in subsection 2.7).

2.7 V^0 particles from the underlying event

In order to extract the V^0 yield in the underlying event (not associated to the hard scatterings tagged by the charged jets considered in this analysis) several estimators have been investigated:

- the so-called *outside cone* (OC) selection: the V^0 particles that were not matched to any jet considered in the analysis within events containing a jet such that $\Delta R_{\mathrm{V}^0-\mathrm{jet}} > R_{\mathrm{cut}}$;
- the *perpendicular cones* (PC) selection: the V^0 particles found at azimuthal angles larger than R_{cut} $\Delta\varphi > R_{\mathrm{cut}}$, where $\Delta\varphi = \varphi^{\mathrm{jet}} - \varphi^{\mathrm{V}^0}$ (say the value)
- the *non-jet events* (NJ) selection: the V^0particles found in events that do not contain a jet with $p_{\mathrm{T}}^{\mathrm{jet}} > 5\mathrm{GeV}/c$.

In practice, a useful quantity for performing the subtraction of the non-jet contribution of the V^0 particles is their density per unit area

$$\rho^{\mathrm{V}^0}(p_{\mathrm{T}}) = N^{\mathrm{V}^0}(p_{\mathrm{T}})/A^{\mathrm{V}^0} \quad (2)$$

, where N^{V^0} is the number of particles and A^{V^0} is the acceptance in pseudo-rapidity and azimuthal angle. Consequently, the number of the UE V^0 particles within a jet can be calculated as $N = \rho^{\mathrm{V}^0} A^{\mathrm{jet}}$ for each estimator separately. Note, in this analysis we consider the jet area $A^{\mathrm{jet}} = \pi R^2$. Depending on the background estimator several estimators for the density of V^0 particles within jets (JC) can be considered such that $\rho_{\mathrm{JC}}^{\mathrm{V}^0} = \rho_{\mathrm{JC,raw}}^{\mathrm{V}^0} - \rho_{\mathrm{UE}}^{\mathrm{V}^0}$, where UE can be any of the OC, PC, NJ. In this analysis we choose PC as the reference and use OC and NJ for the systematic uncertainty estimation.

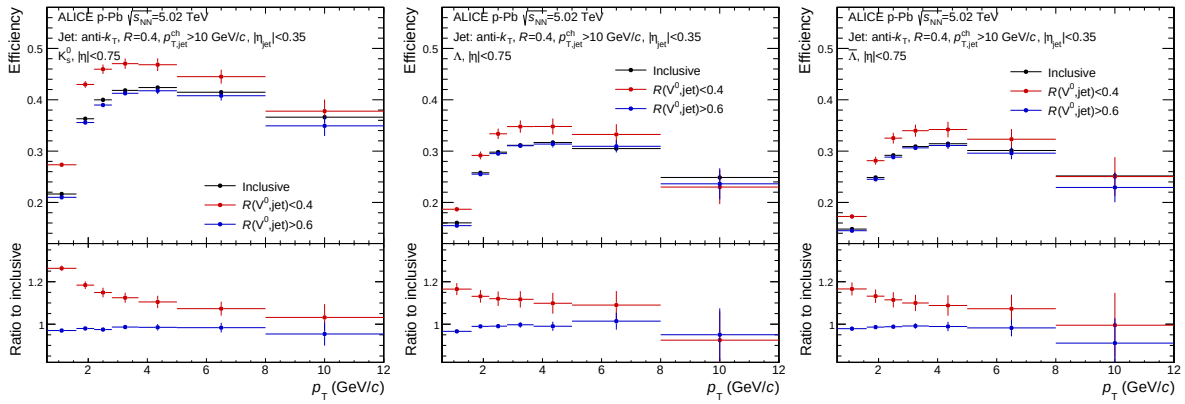

Fig. 1: Efficiency of V^0 particles for three selections: inclusice, within the radius of 0.4 from the jet axis, and at larger radii $R > 0.6$ away from the jet axis.

2.8 V^0 reconstruction efficiency

The efficiencies of V^0particles were estimated using DPMJET Monte Carlo generator [50] with the same cuts as in the data except the daughter track PID with dE/dx in TPC.

Due to differences in the experimental acceptance for V^0 particles associated to jets (JC) and those extracted through the various estimators of the underlying event (OC, PC, NJ) the efficiencies of V^0 particles were estimated separately for every case. Figure 1 shows the inclusive reconstruction efficiency for V^0 particles and the efficiency in the events containing a jet for two selections of distance R from the main jet axis. The efficiency within events conaining a jet varies with R and for every selection of R the efficiencies were evaluated separately.

2.9 Feed-down subtraction for Λ and $\overline{\Lambda}$

The p_T differential yields of Λ and $\overline{\Lambda}$ reconstructed for each selection (JC and UE selections) where corrected for the feed-down from Ξ decays. The Ξ production in jets (JC) was estimated based on measurements of the multi-strange baryons and their decays at high-p_T performed in pp collisions [51] and extrapolated to the lower p_T using PYTHIA event generator and full detector simulations. The applied correction is of about 15% and largely independent of the Λ and $\overline{\Lambda}$ momentum. check numbers Conversely, Λyields were not corrected for the feed-down from Ω^- baryons nor for the feed-down from non-weak decays of Ξ^0 and $\Xi(1385)$ family as these contributions are neglibible as compared to the systematic uncertainties of the present measurement.

2.10 Systematic uncertainties

The systematic uncertainties on the particle spectra and their ratios originating from the sources discussed below are added in quadrature.

The main sources in the V^0 particle reconstruction are the level of knowledge of detector materials (resulting in a 4% uncertainty), track selections (up to 5%) and the feed-down correction for the Λ (5%), while topological selections contribute 2-4% depending on transverse momentum. These systematic uncertainties are summarized in Table 2 and presented in Fig. 2.

Two main sources of uncertainties originating from the mis-association of V^0particles with UE

	K^0_S	$\Lambda(\bar{\Lambda})$	
Proper lifetime	2%	2%	
Material budget	4%	4%	
Track selection	4%	4%	
TPC PID	1%	1%	
p_{T} (GeV/c)		< 3.7	> 3.7
Feed-down correction		5%	7%
p_{T} (GeV/c)		< 3.7	> 3.7
Total	6.5%	8%	9.5%

Table 2: Main sources of systematic uncertainty for the K^0_S and $\Lambda(\bar{\Lambda})$.

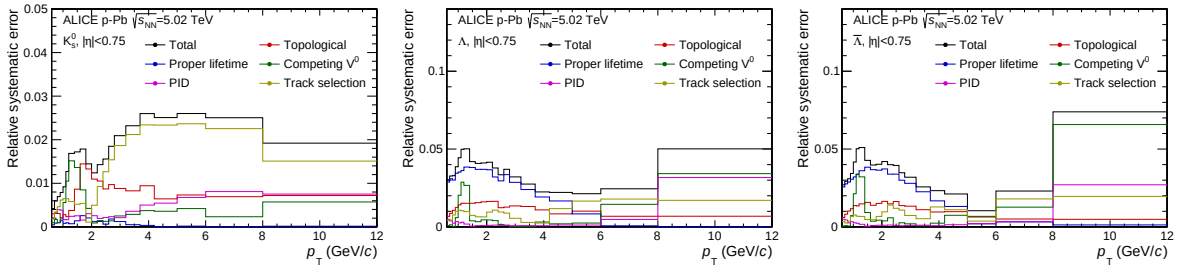

Fig. 2: Systematic uncertainties on V^0 particle spectrum (left: K^0_S), center: Λ, right: $\bar{\Lambda}$) as a function of their transverse momentum (see text and Tab. 2 for details).

were considered:

- the V^0 particle was found outside the selected jet and classified as UE particle; however, it may have originated by a physical jet outside the fiducial acceptance for jets considered in the analysis and/or from a *true* low-p_{T} jet, below the considered thresholds;
- the V^0 particle originates from true high-p_{T}jet; however, due to the finite detector efficiency the jet has not been reconstructed above the considered p_{T} threshold.

The uncertainty on the UE V^0 density has been estimated using the two variations of the UE estimators: the so-called *outside cone* (OC) and the *non-jet events* (NJ). The OC and the NJ estimators encapsulate the maximum deviation in the yield of UE particles and the difference of the reconstructed V^0 yields in OC and NJ has been included as the additional systematic uncertainties on the density of particles within the jets (JC). The uncerainty is largest for low-momenta particles ($< 2\mathrm{GeV}/c$) reaching up to 30% but drops rapidly with $p_{\mathrm{T}}$to negligible values at $6\mathrm{GeV}/c$. check numbers .

The systematic uncertainty originating from the selection of the jet p_{T} were estimated by repeating the analysis with jet p_{T} varied around the chosen thresholds of 10 and 20 GeV/c by 2 GeV/c. This variation accounts for jet resolution due to detector effects and the fluctuations

of the event background density as reported in [24]. It reaches up to 10% at low momenta ($< 2\text{GeV}/c$) and remains almost a constant 5% for $p_{\mathrm{T}} > 2\text{GeV}/c$. check numbers

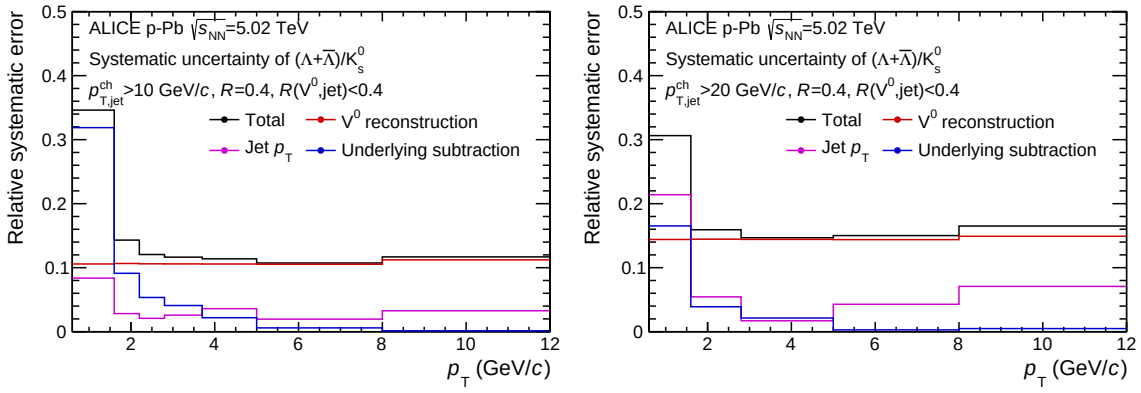

Fig. 3: Relative systematic uncertainty on the ratio of Λ and $\mathrm{K}^0_{\mathrm{S}}$ spectrum within $R = 0.4$ anti-k_{T} jets for $p_{\mathrm{T,ch\,jet}} > 10\text{GeV}/c$ (left) and $p_{\mathrm{T,ch\,jet}} > 20\text{GeV}/c$ (right) as a function of particle p_{T}. Three contributions to the total uncertainty are shown: uncertainty on V^0 reconstruction, uncertainty on the underlying event subtraction, and uncertainty on the jet momentum scale and momentum resolution.

Figure 3 shows the relative systematic uncertainties on the $\Lambda/\mathrm{K}^0_{\mathrm{S}}$ ratio reconstructed within $R = 0.4$ jets with $p_{\mathrm{T,ch\,jet}} > 10\text{GeV}/c$ and $p_{\mathrm{T,ch\,jet}} > 20\text{GeV}/c$ as a function of particles p_{T}. For the $p_{\mathrm{T,ch\,jet}} > 20\text{GeV}/c$ the total uncertainty is about 16% and largely independent of particle p_{T} with the largest contribution 14% from the uncertainty on V^0 reconstruction.

3 Results

3.1 p_{T} density

The fully corrected densities of $\mathrm{K}^0_{\mathrm{S}}$ and the sum of Λ and $\overline{\Lambda}$ particles associated to a hard scattering tagged by an energetic jet are shown in Fig. 4. The per jet density within the jet cone (JC) is compared to the density for inclusive particles (without association to jets) and to the density in the perpendicular cones (PC). In the case of inclusive particles the distribution is normalized to the product of the total number of events and the acceptance of the V^0 particles in a single event (full azimuth and $|\eta| < 0.75$). As expected, for both $\mathrm{K}^0_{\mathrm{S}}$ and Λ particles the density within jets is much harder as the high-p_{T} particles originate from energetic jets. The density in the PC selection is qualitatively similar to the inclusive distribution showing strong p_{T} dependence. Both, the inclusive and the PC distributions show a rapid decrease with p_{T} reaching values more than an order of magnitude lower than the JC density for particle p_{T} exceeding $4\text{GeV}/c$. This is consistent with an expectation that the high-p_{T} particles originate from energetic jet fragmentation.

3.2 L/K ratios

Ratios of Λ and $\mathrm{K}^0_{\mathrm{S}}$ yields can be obtained by dividing the normalized density distributions. In the following the sum of Λ and $\overline{\Lambda}$ densities is divided by the density of $\mathrm{K}^0_{\mathrm{S}}$. Moreover, as no significant difference was found for different jet resolution parameters R the results are presented as the average of results obtained with R of 0.2, 0.3, and 0.4. Figure 5 shows the ratio for the JC selection as a function of the distance from the jet axis $R(\mathrm{V}^0, jet)$ without subtracting the UE backgrounds. The ratio is shown for three momentum bins: the low-p_{T}

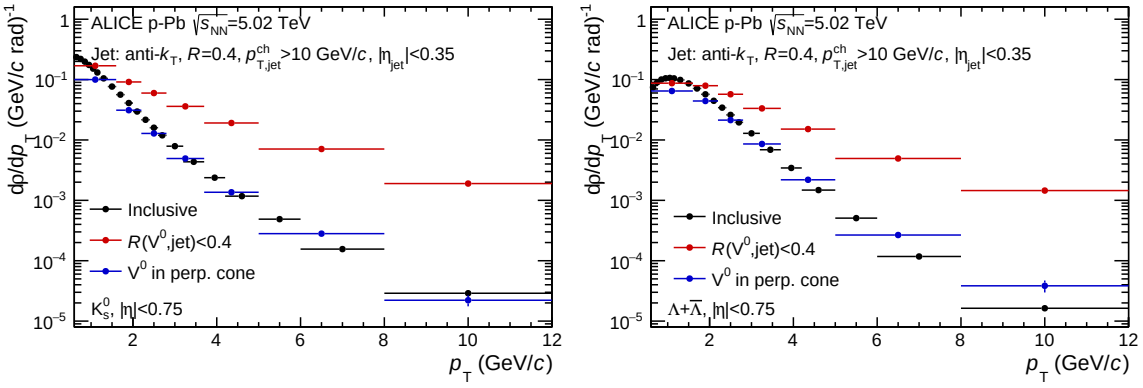

Fig. 4: Differencial density of particles $\mathrm{d}\rho^{\mathrm{V}^0}/\mathrm{d}p_{\mathrm{T}}$ (see Eq. 2) for $\mathrm{K}^0_{\mathrm{S}}$ (left) and Λ (right). Density is shown for three selections: inclusive particles from minimum bias events, particles within an energetic ($p_{\mathrm{T}} > 10\mathrm{GeV}/c$) anti-$k_{\mathrm{T}}$ jet with $R = 0.4$ and the perpendicular cones (PC) within the events that an energetic jet was found.

($0.6 < p_{\mathrm{T}} < 1.8\mathrm{GeV}/c$), inermediate p_{T} ($2.2 < p_{\mathrm{T}} < 3.7\mathrm{GeV}/c$), and the high-$p_{\mathrm{T}}$ ($4.2 < p_{\mathrm{T}} < 12\mathrm{GeV}/c$). The ratio as a function of $R(\mathrm{V}^0,jet)$ at low-p_{T} remains approximately constant at about 0.2 independent of the distance to the jet axis and that is the case even at large distances of $R(\mathrm{V}^0,jet) > 1.2$. This value is consistent with the inclusive measurements in p–Pbcollisions, but also in pp and peripheral Pb–Pb collisions were effects related to the collective expansion of the system are either not-present or small [52].

Conversely the intermediate-p_{T} selection shows an increase of the ratio from about 0.3 when evaluated close to the jet axis to values of about 0.6 at $R(\mathrm{V}^0,jet)$ distances of about 0.5. For distances $R(\mathrm{V}^0,jet) > 0.5$ the ratio remains constant. The ratio of 0.6 is consistent with the inclusive measurement in p–Pb collisions [20] and this p_{T} region is where the ehnanced $\Lambda/\mathrm{K}^0_{\mathrm{S}}$ ratio in the inclusive measurements was found the largest. We stress that for the results shown in Fig. 5 the UE backgrounds were not subtracted. Therefore the evolution of the ratio as a function of the distance from the axis demonstrates how the two sources UE and energetic jet compete. The lack of enhancement (values consistent with pp collisions) close to the jet axis indicate that the enhanced $\Lambda/\mathrm{K}^0_{\mathrm{S}}$ ratio is not associated with the energetic jets.

In each of the momentum bins the ratio is dominated by the lower edge of the selection window. This is especially the case for the high-p_{T} selection where the dominating component originates from $p_{\mathrm{T}}$of about $4.5\mathrm{GeV}/c$ and tje $R(\mathrm{V}^0,jet)$ dependence at high-p_{T} is similar to intermediate p_{T}. The ratio at high-p_{T} accociated to jets is discussed below.

The right panel of Fig.5 shows the ratio of Λ to $\mathrm{K}^0_{\mathrm{S}}$ as a function of particle p_{T} for four selections: the inclusive particles, the particles from the PC selection, and two JC selections for jet p_{T} of 10 and $20\mathrm{GeV}/c$ averaged over three resolution parameters R (0.2, 0.3, 0.4). For JC selection, prior to forming the ratio, the UE density contribution obtained with the PC selection was subtracted from the JC densities for each particle species separately. Additionally, for the results in Fig. 5 every V^0 particle was required to be close to the jet axis with its distance $R(\mathrm{V}^0,jet) < 0.2$. The inclusive and the PC distributions show the enahncement at p_{T} of about $3\mathrm{GeV}/c$. The ratio for the inclusive case is consistent with the measurement presented in [20]. The PC distribution above $2\mathrm{GeV}/c$ reaches systematically higher values than the inclusive. The Λ-to-$\mathrm{K}^0_{\mathrm{S}}$ ratio within jets is consistently is lower than the inclusive case and approximately independent of p_{T} beyond $2\mathrm{GeV}/c$. In particular, the ratio for particles associated to the jet does not show a maximum

at the intermediate p_{T}. This coroborates the scenario in which the enhancement of $\Lambda/\mathrm{K}^0_{\mathrm{S}}$ is not present within jets. Additionally, this conclusion holds for both, 10GeV$/c$but also higher p_{T} (20GeV$/c$) jets.

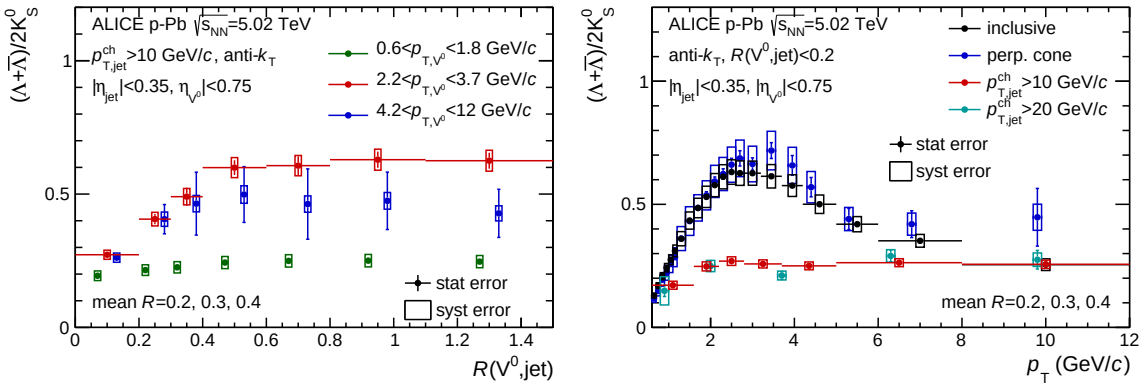

Fig. 5: Ratio of Λ and $\mathrm{K}^0_{\mathrm{S}}$ yields for three selections

the following is to be reworked or removed all together - it is a comment and not altering any of the conclusions: Selecting hard scatterings according to the jet energy carried exclusively by the primary charged particles induces biases and inefficiencies on the jet spectrum. The bias is related to the probabilistic process of fragmentation and hadronization. This analysis will not tag parton showers that fragmented into a configuration of hadrons that did resulted in producing a 10 GeV charged particle jet with a given R. Therefore, there can be cases of V^0 particles that originated from a parton of a hard scattering but were not associated to a charged particle jet. Using PYTHIA simulations we found that the most probable p_{T} of the full jet energy is larger by about 40%. Moreover, since the daughters of the V^0 particles are not included in the jet energy calculation there are cases of jets containig V^0 particles but not included in this analysis. However, the right panel of Fig. 5 shows that the inclusive $\Lambda/\mathrm{K}^0_{\mathrm{S}}$ ratio at high-p_{T} is fully consistent with the ratio from particles associated to jets in this analysis.

4 Summary

In conclusion, the enhancement in the ratio of inlcusive Λ, $\overline{\Lambda}$ and $\mathrm{K}^0_{\mathrm{S}}$ found in the p–Pb and Pb–Pb collisions is not present for particles associated to a hard scattering.

from the PbPb paper: The agreement between collision systems suggests that the relative fragmentation into Λ and $\mathrm{K}^0_{\mathrm{S}}$ hadrons at high pT, even in central collisions, is vacuum-like and not modified by the medium.

As such enhancement has been linked to the interplay of radial flow and parton recombination at intermediate-p_{T} its absence within the jet cone demonstrates that these effects are confined to a soft particle production and do not modify jet composition.

Acknowledgements

References

[1] H. Satz, "Color deconfinement in nuclear collisions," *Rept.Prog.Phys.* **63** (2000) 1511, arXiv:hep-ph/0007069 [hep-ph].

[2] S. Bass, M. Gyulassy, H. Stoecker, and W. Greiner, "Signatures of quark gluon plasma formation in high-energy heavy ion collisions: A Critical review," *J.Phys.* **G25** (1999) R1–R57, arXiv:hep-ph/9810281 [hep-ph].

[3] E. V. Shuryak, "THEORY AND PHENOMENOLOGY OF THE QCD VACUUM. 7. MACROSCOPIC EXCITATIONS," *Phys.Rept.* **115** (1984) 151.

[4] J. Cleymans, R. Gavai, and E. Suhonen, "Quarks and Gluons at High Temperatures and Densities," *Phys.Rept.* **130** (1986) 217.

[5] S. Borsanyi, G. Endrodi, Z. Fodor, A. Jakovac, S. D. Katz, *et al.*, "The QCD equation of state with dynamical quarks," *JHEP* **1011** (2010) 077, arXiv:1007.2580 [hep-lat].

[6] T. Bhattacharya, M. I. Buchoff, N. H. Christ, H.-T. Ding, R. Gupta, *et al.*, "QCD Phase Transition with Chiral Quarks and Physical Quark Masses," *Phys.Rev.Lett.* **113** no. 8, (2014) 082001, arXiv:1402.5175 [hep-lat].

[7] B. Muller and J. L. Nagle, "Results from the relativistic heavy ion collider," *Ann.Rev.Nucl.Part.Sci.* **56** (2006) 93–135, arXiv:nucl-th/0602029 [nucl-th].

[8] E. Schnedermann, J. Sollfrank, and U. W. Heinz, "Thermal phenomenology of hadrons from 200-A/GeV S+S collisions," *Phys.Rev.* **C48** (1993) 2462–2475, arXiv:nucl-th/9307020 [nucl-th].

[9] **PHOBOS** Collaboration, B. Alver *et al.*, "Phobos results on charged particle multiplicity and pseudorapidity distributions in Au+Au, Cu+Cu, d+Au, and p+p collisions at ultra-relativistic energies," *Phys.Rev.* **C83** (2011) 024913, arXiv:1011.1940 [nucl-ex].

[10] **CMS** Collaboration, V. Khachatryan *et al.*, "Observation of Long-Range Near-Side Angular Correlations in Proton-Proton Collisions at the LHC," *JHEP* **1009** (2010) 091, arXiv:1009.4122 [hep-ex].

[11] **CMS** Collaboration, S. Chatrchyan *et al.*, "Observation of long-range near-side angular correlations in proton-lead collisions at the LHC," *Phys.Lett.* **B718** (2013) 795–814, arXiv:1210.5482 [nucl-ex].

[12] **ALICE** Collaboration, B. Abelev *et al.*, "Long-range angular correlations on the near and away side in p-Pb collisions at $\sqrt{s_{NN}} = 5.02$ TeV," *Phys.Lett.* **B719** (2013) 29–41, arXiv:1212.2001 [nucl-ex].

[13] **ATLAS** Collaboration, G. Aad *et al.*, "Observation of Associated Near-Side and Away-Side Long-Range Correlations in $\sqrt{s_{NN}}$=5.02 TeV Proton-Lead Collisions with the ATLAS Detector," *Phys.Rev.Lett.* **110** no. 18, (2013) 182302, arXiv:1212.5198 [hep-ex].

[14] **ATLAS** Collaboration, G. Aad *et al.*, "Measurement with the ATLAS detector of multi-particle azimuthal correlations in p+Pb collisions at *sqrt*(s_{NN})=5.02 TeV," *Phys.Lett.* **B725** (2013) 60–78, arXiv:1303.2084 [hep-ex].

[15] **CMS** Collaboration, S. Chatrchyan *et al.*, "Multiplicity and transverse momentum dependence of two- and four-particle correlations in pPb and PbPb collisions," *Phys.Lett.* **B724** (2013) 213–240, arXiv:1305.0609 [nucl-ex].

[16] K. Dusling and R. Venugopalan, "Comparison of the color glass condensate to dihadron correlations in proton-proton and proton-nucleus collisions," *Phys.Rev.* **D87** no. 9, (2013) 094034, arXiv:1302.7018 [hep-ph].

[17] P. Bozek and W. Broniowski, "Correlations from hydrodynamic flow in p-Pb collisions," *Phys.Lett.* **B718** (2013) 1557–1561, arXiv:1211.0845 [nucl-th].

[18] G.-Y. Qin and B. M?ller, "Elliptic and triangular flow anisotropy in deuteron-gold collisions at $\sqrt{s_{NN}} = 200$ GeV at RHIC and in proton-lead collisions at $\sqrt{s_{NN}} = 5.02$ TeV at the LHC," *Phys.Rev.* **C89** no. 4, (2014) 044902, arXiv:1306.3439 [nucl-th].

[19] A. Bzdak, B. Schenke, P. Tribedy, and R. Venugopalan, "Initial state geometry and the role of hydrodynamics in proton-proton, proton-nucleus and deuteron-nucleus collisions," *Phys.Rev.* **C87** no. 6, (2013) 064906, arXiv:1304.3403 [nucl-th].

[20] **ALICE** Collaboration, B. B. Abelev *et al.*, "Multiplicity Dependence of Pion, Kaon, Proton and Lambda Production in p-Pb Collisions at $\sqrt{s_{NN}}$ = 5.02 TeV," *Phys.Lett.* **B728** (2014) 25–38, arXiv:1307.6796 [nucl-ex].

[21] **ALICE** Collaboration, B. B. Abelev *et al.*, "K^0_S and Λ production in Pb-Pb collisions at $\sqrt{s_{NN}}$ = 2.76 TeV," *Phys.Rev.Lett.* **111** (2013) 222301, arXiv:1307.5530 [nucl-ex].

[22] **ALICE** Collaboration, B. B. Abelev *et al.*, "Long-range angular correlations of π, K and p in p-Pb collisions at $\sqrt{s_{\rm NN}}$ = 5.02 TeV," *Phys.Lett.* **B726** (2013) 164–177, arXiv:1307.3237 [nucl-ex].

[23] R. Fries, B. Muller, C. Nonaka, and S. Bass, "Hadronization in heavy ion collisions: Recombination and fragmentation of partons," *Phys.Rev.Lett.* **90** (2003) 202303, arXiv:nucl-th/0301087 [nucl-th].

[24] **ALICE** Collaboration, J. Adam *et al.*, "Measurement of charged jet production cross sections and nuclear modification in p-Pb collisions at $\sqrt{s_{\rm NN}} = 5.02$ TeV," arXiv:1503.00681 [nucl-ex].

[25] **ALICE** Collaboration, J. Adam *et al.*, "Measurement of dijet $k_{\rm T}$ in p-Pb collisions at $\sqrt{s_{\rm NN}} = \mathbf{5.02}$ TeV," arXiv:1503.03050 [nucl-ex].

[26] L. D. McLerran, "The Color glass condensate and small x physics: Four lectures," *Lect.Notes Phys.* **583** (2002) 291–334, arXiv:hep-ph/0104285 [hep-ph].

[27] C. Salgado, J. Alvarez-Muniz, F. Arleo, N. Armesto, M. Botje, *et al.*, "Proton-Nucleus Collisions at the LHC: Scientific Opportunities and Requirements," *J.Phys.* **G39** (2012) 015010, arXiv:1105.3919 [hep-ph].

[28] A. Krzywicki, J. Engels, B. Petersson, and U. Sukhatme, "Does a Nucleus Act Like a Gluon Filter?," *Phys.Lett.* **B85** (1979) 407.

[29] A. Accardi, "Final state interactions and hadron quenching in cold nuclear matter," *Phys.Rev.* **C76** (2007) 034902, arXiv:0706.3227 [nucl-th].

[30] **ATLAS** Collaboration, G. Aad *et al.*, "Observation of a Centrality-Dependent Dijet Asymmetry in Lead-Lead Collisions at $\sqrt{s_{NN}} = 2.77$ TeV with the ATLAS Detector at the LHC," *Phys.Rev.Lett.* **105** (2010) 252303, arXiv:1011.6182 [hep-ex].

[31] **CMS** Collaboration, S. Chatrchyan *et al.*, "Jet momentum dependence of jet quenching in PbPb collisions at $\sqrt{s_{NN}} = 2.76$ TeV," *Phys.Lett.* **B712** (2012) 176–197, arXiv:1202.5022 [nucl-ex].

[32] **ATLAS** Collaboration, G. Aad *et al.*, "Measurement of the jet radius and transverse momentum dependence of inclusive jet suppression in lead-lead collisions at $\sqrt{s_{NN}}$= 2.76 TeV with the ATLAS detector," *Phys.Lett.* **B719** (2013) 220–241, arXiv:1208.1967 [hep-ex].

[33] **ALICE** Collaboration, B. Abelev *et al.*, "Measurement of charged jet suppression in Pb-Pb collisions at $\sqrt{s_{NN}}$ = 2.76 TeV," *JHEP* **1403** (2014) 013, arXiv:1311.0633 [nucl-ex].

[34] **ATLAS** Collaboration, G. Aad *et al.*, "Measurements of the Nuclear Modification Factor for Jets in Pb+Pb Collisions at $\sqrt{s_{\rm NN}} = 2.76$ TeV with the ATLAS Detector," *Phys.Rev.Lett.* **114** no. 7, (2015) 072302, arXiv:1411.2357 [hep-ex].

[35] **ALICE Collaboration** Collaboration, K. Aamodt *et al.*, "The ALICE experiment at the CERN LHC," *JINST* **3** (2008) S08002.

[36] L. Evans and P. Bryant, "LHC Machine," *JINST* **3** (2008) S08001.

[37] **ALICE** Collaboration, K. Aamodt *et al.*, "Alignment of the ALICE Inner Tracking System with cosmic-ray tracks," *JINST* **5** (2010) P03003, arXiv:1001.0502 [physics.ins-det].

[38] J. Alme, Y. Andres, H. Appelshauser, S. Bablok, N. Bialas, *et al.*, "The ALICE TPC, a large 3-dimensional tracking device with fast readout for ultra-high multiplicity events," *Nucl.Instrum.Meth.* **A622** (2010) 316–367, arXiv:1001.1950 [physics.ins-det].

[39] A. Akindinov, A. Alici, A. Agostinelli, P. Antonioli, S. Arcelli, *et al.*, "Performance of the ALICE Time-Of-Flight detector at the LHC," *Eur.Phys.J.Plus* **128** (2013) 44.

[40] **ALICE** Collaboration, E. Abbas *et al.*, "Performance of the ALICE VZERO system," *JINST* **8** (2013) P10016, arXiv:1306.3130 [nucl-ex].

[41] **ALICE** Collaboration, B. Abelev *et al.*, "Pseudorapidity density of charged particles in p + Pb collisions at $\sqrt{s_{NN}} = 5.02$ TeV," *Phys.Rev.Lett.* **110** no. 3, (2013) 032301, arXiv:1210.3615 [nucl-ex].

[42] **ALICE** Collaboration, B. B. Abelev *et al.*, "Performance of the ALICE Experiment at the CERN LHC," *Int.J.Mod.Phys.* **A29** (2014) 1430044, arXiv:1402.4476 [nucl-ex].

[43] M. Cacciari, G. P. Salam, and G. Soyez, "The Anti-k(t) jet clustering algorithm," *JHEP* **0804** (2008) 063, arXiv:0802.1189 [hep-ph].

[44] M. Cacciari, G. P. Salam, and G. Soyez, "FastJet User Manual," *Eur.Phys.J.* **C72** (2012) 1896, arXiv:1111.6097 [hep-ph].

[45] M. Cacciari and G. P. Salam, "Dispelling the N^3 myth for the k_t jet-finder," *Phys.Lett.* **B641** (2006) 57–61, arXiv:hep-ph/0512210 [hep-ph].

[46] M. Cacciari, G. P. Salam, and G. Soyez, "The Catchment Area of Jets," *JHEP* **0804** (2008) 005, arXiv:0802.1188 [hep-ph].

[47] **ALICE** Collaboration, J. Adam *et al.*, "Measurement of jet suppression in central Pb-Pb collisions at $\sqrt{s_{\rm NN}}$ = 2.76 TeV," *Phys.Lett.* **B746** (2015) 1–14, arXiv:1502.01689 [nucl-ex].

[48] **Particle Data Group** Collaboration, B. D. Fields, P. Molaro, and S. Sarkar, "Big-bang nucleosynthesis," *Chin.Phys.* **C38** (2014) 090001, arXiv:1412.1408 [astro-ph].

[49] **ALICE** Collaboration, K. Aamodt *et al.*, "Strange particle production in proton-proton collisions at sqrt(s) = 0.9 TeV with ALICE at the LHC," *Eur.Phys.J.* **C71** (2011) 1594, arXiv:1012.3257 [hep-ex].

[50] S. Roesler, R. Engel, and J. Ranft, "The Monte Carlo event generator DPMJET-III," arXiv:hep-ph/0012252 [hep-ph].

[51] **ALICE** Collaboration, B. Abelev *et al.*, "Multi-strange baryon production in pp collisions at $\sqrt{s} = 7$ TeV with ALICE," *Phys.Lett.* **B712** (2012) 309–318, arXiv:1204.0282 [nucl-ex].

[52] **ALICE** Collaboration, B. B. Abelev *et al.*, "$K^*(892)^0$ and ?(1020) production in Pb-Pb collisions at $\sqrt{s_{NN}}$=2.76 TeV," *Phys.Rev.* **C91** no. 2, (2015) 024609, arXiv:1404.0495 [nucl-ex].

A The ALICE Collaboration